

Broadband Nanoscale Surface-Enhanced Raman Spectroscopy by Multiresonant Nanolaminate Plasmonic Nanocavities on Vertical Nanopillars

Meitong Nie, Yuming Zhao, Wonil Nam, Junyeob Song, Wenqi Zhu, Henri J. Lezec, Amit Agrawal, and Wei Zhou*

Surface-enhanced Raman spectroscopy (SERS) has become a sensitive detection technique for biochemical analysis. Despite significant research efforts, most SERS substrates consisting of single-resonant plasmonic nanostructures on the planar surface suffer from limitations of narrowband SERS operation and unoptimized nano-bio interface with living cells. Here, it is reported that nanolaminate plasmonic nanocavities on 3D vertical nanopillar arrays can support a broadband SERS operation with large enhancement factors ($>10^6$) under laser excitations at 532, 633, and 785 nm. The multi-band Raman mapping measurements show that nanolaminate plasmonic nanocavities on vertical nanopillar arrays exhibit broadband uniform SERS performance with diffraction-limited resolution at a single nanopillar footprint. By selective exposure of embedded plasmonic hotspots in individual metal-insulator-metal (MIM) nanogaps, nanoscale broadband SERS operation at the single MIM nanocavity level with visible and near-infrared (vis-NIR) excitations is demonstrated. Numerical studies reveal that nanolaminate plasmonic nanocavities on vertical nanopillars can support multiple hybridized plasmonic modes to concentrate optical fields across a broadband wavelength range from 500 to 900 nm at the nanoscale.

show that multi-band SERS measurements under multiple excitation wavelengths can empower multiplexed detection of multiple analytes for complex samples.^[3] In this regard, it is highly desirable to develop broadband multiresonant plasmonic systems for multi-band SERS measurements under different laser excitations. Notably, by spectrally matching the wavelengths among the excitation laser, plasmon resonance, and analyte absorption peak, multiresonant plasmonic systems can allow the surface-enhanced resonant Raman spectroscopy (SRRS) with an extra 10- to 100-fold signal intensity increment than the nonresonant SERS.^[3c,4] Since analyte molecules possess characteristic electronic transition features in addition to their vibrational fingerprints, multi-band SERS measurements under multiple excitation wavelengths can provide combined electronic and vibrational spectral information to enable a higher dimensional biochemical analysis of complex samples with multiple analytes.^[3a]

1. Introduction


Surface-enhanced Raman spectroscopy (SERS), combining the molecular fingerprinting specificity of vibrational spectroscopy with the hotspot sensitivity of plasmonic nanostructures, can serve as an ultrasensitive bioanalytical detection technique.^[1] Conventional SERS substrates with single-resonant plasmonic nanostructures can provide high SERS enhancement factors (EFs $> 10^6$) within a restricted excitation wavelength range.^[2] Recent studies

For SERS bioanalysis of living cells, it is imperative to achieve intimate interfacing of plasmonic hotspots with the cell membrane^[5] to enable direct probing of membrane organelles^[6] and minimally invasive intracellular nanosurgery.^[7] Recent studies have shown that protruding nanopillar structures with large local curvatures can activate mammalian cell engulfment machinery to promote an intimate nanodevice-cell coupling.^[8] Notably, vertical nanopillar nanoelectrodes can trigger cellular engulfment activities for neurons and cardiomyocytes to create a tight resistive sealing and achieve intracellular-like electrical signal recording.^[9] Unfortunately, existing nanopillar-shaped plasmonic nanostructures, such as hollow metal nano-straws,^[10] 3D nanowire-like structures,^[11] vertically aligned carbon nanotubes,^[12] and mushroom-shaped vertical structures,^[13] still face the design-fabrication constraints for seamless integration of multiresonant plasmonic nanostructures with predefined nanopillar array in multi-band SERS sensing of living cells.

The current design strategy for multi-band SERS substrates is to densely pack multiple plasmonic building blocks with different resonant wavelengths, such as different-sized Ag nanoparticles on glass-Ag-glass multilayers,^[14] different-shaped plasmonic metal nanoparticles on Ag gratings,^[15] random Ag

M. Nie, Y. Zhao, W. Nam, W. Zhou
Department of Electrical and Computer Engineering
Virginia Tech
Blacksburg, VA 24061, USA
E-mail: wzhu@vt.edu

J. Song, W. Zhu, H. J. Lezec, A. Agrawal
Physical Measurement Laboratory
National Institute of Standards and Technology
Gaithersburg, MD 20899, USA

 The ORCID identification number(s) for the author(s) of this article can be found under <https://doi.org/10.1002/adfm.202202231>.

DOI: 10.1002/adfm.202202231

nanoparticles on Au nano-bow arrays,^[16] and width-graded arrays of plasmonic nanogratings.^[17] Despite the simplicity in fabrication, these multi-band SERS substrates suffer from several limitations to integrate with nanopillars, including: 1) large footprint due to the in-plane arrangement of multiple plasmonic building blocks; 2) limited spatial overlaps of different plasmonic modes; 3) difficult geometric control of plasmonic resonance properties; and 4) poor spatial uniformity of SERS hotspots.

In this study, we first characterized the multi-band SERS performance of the nanolaminate plasmonic nanocavities on high-aspect-ratio nanopillar arrays under laser excitations at 532, 633, and 785 nm. Next, we partially etched the dielectric layers and exposed the embedded hotspots in the nanocavities to analytes, leading to several times improvement in SERS enhancement factors (EFs) in multi-band SERS measurements. Then, we selectively etched one individual dielectric layer and observed that the spatial mode distribution among three metal–insulator–metal (MIM) nanogaps strongly depends on excitation laser wavelength. Last, numerical simulation studies revealed that the observed nanoscale broadband SERS performance is due to multiple spectrally separated and spatially overlapped hybrid plasmonic modes in nanolaminate plasmonic nanocavities over a broad vis–NIR spectral range. Our results show that multiresonant nanolaminate plasmonic nanocavities on high-aspect-ratio nanopillar arrays allow high-performance multi-band SERS operation between 500 and 900 nm at the single nanocavity level (Figure 1A). Compared with conventional planar or low-aspect-ratio plasmonic nanostructures,^[18] multiresonant nanolaminate plasmonic nanocavities on high-aspect-ratio vertical nanopillars can provide unique opportunities. First, the out-of-plane geometric engineering of vertically stacked nanolaminate plasmonic nanocavities can allow for precise and dense stacking of broadband multiresonant and spatially overlapped SERS hotspots within a nanoscale footprint. Second, integrating multiresonant plasmonic nanodevices with high-aspect-ratio nanopillars can activate engulfment machinery at the bio-nano interface for living mammalian cells, improving the SERS bioanalytical performance.^[5] Third, nanolaminate plasmonic nanocavities can be integrated with

predefined nanopillar electrode arrays for combined electrical recording and SERS monitoring of living cells. Fourth, multiresonant plasmonic nanodevices with spatial overlaps can potentially enable wavelength-multiplexed multifunctional nanophotonics and multiphoton nonlinear plasmonics.^[19]

2. Result and Discussion

Figure 1B illustrates the top-down scalable fabrication process to create Ag/SiO₂/Ag nanolaminate plasmonic nanostructures on predefined vertical nanopillar arrays. Briefly, the predefined polyurethane (PU) polymer nanopillar array with a diameter of ≈100 nm, a height of ≈400 nm, and a pitch size of ≈400 nm was replicated from nanowell-array structured polydimethylsiloxane (PDMS) stamp by nanoimprinting lithography. Next, we employed physical vapor evaporation to deposit alternating thin films of Ag (≈30 nm thickness) and SiO₂ (≈6, ≈8, and ≈12 nm thicknesses from bottom to top, respectively) on the PU nanopillar array, followed by an outer oxidation protection SiO₂ layer (≈30 nm thickness). The dark appearance in the top-view optical image and the vivid diffraction pattern in the tilted-view optical image (Figure 1C) manifest a broadband absorption in the visible range and uniform distribution of nanostructures on the substrate. The top-view and cross-sectional scanning electron microscopy (SEM) images in Figure 1D,E and Figure S1, Supporting Information illustrate the periodic nanopillar structures and multilayered MIM geometries of the fabricated samples. The design and fabrication of plasmonic MIM nanocavities on high-aspect-ratio nanopillars are desirable to achieve intimate interfacing with the cell membrane in biosensing applications. Notably, by wet etching of SiO₂ layers with buffered oxide etchant (BOE), the edges of SiO₂ layers were partially etched away, and the embedded hotspots in MIM nanogaps were exposed to analytes, as shown in Figure 1F. We used an etching time of 15 s to prevent over-etching of SiO₂ layers and maintain the mechanical stability of MIM nanogaps on nanopillars (Figure S2, Supporting Information).

To examine multi-band SERS performance, we measured the SERS spectra from Ag/SiO₂/Ag samples with surface-modified

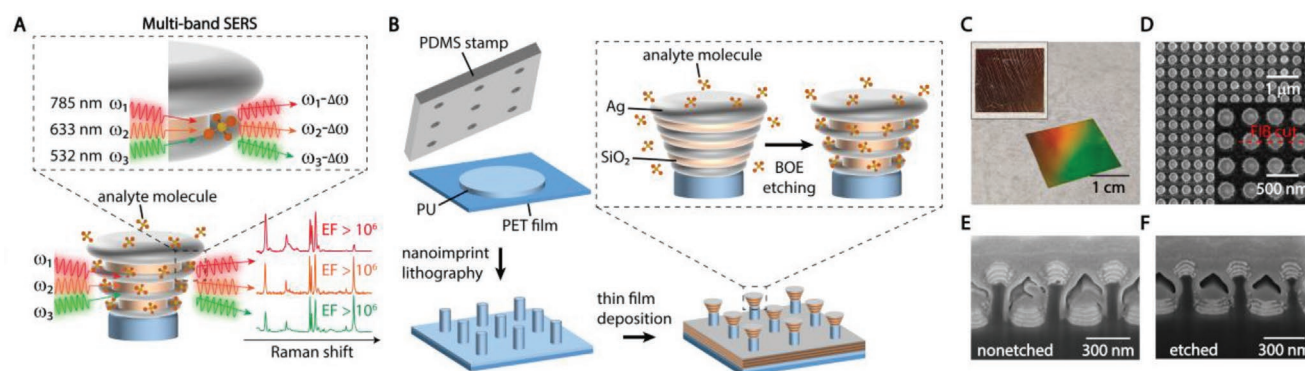


Figure 1. Multiresonant nanolaminate plasmonic nanocavities on vertical nanopillars. A) Scheme of nanoscale multi-band SERS under multiple laser excitations. B) The schematic fabrication process and illustration of Ag/SiO₂/Ag nanolaminate plasmonic nanocavities before and after BOE etching of SiO₂ layers. C) Tilted-view and top-view (inset) optical camera images of the fabricated sample. D) Top-view SEM images of nanolaminate plasmonic nanocavities on vertical nanopillars. E,F) Cross-sectional view SEM images of nanolaminate plasmonic nanocavities on vertical nanopillars before (E) and after (F) 15 s BOE etching of SiO₂ layers. The cutting plane of (E) is marked by the red dashed line labeled as focused ion-beam (FIB) cut in (D).

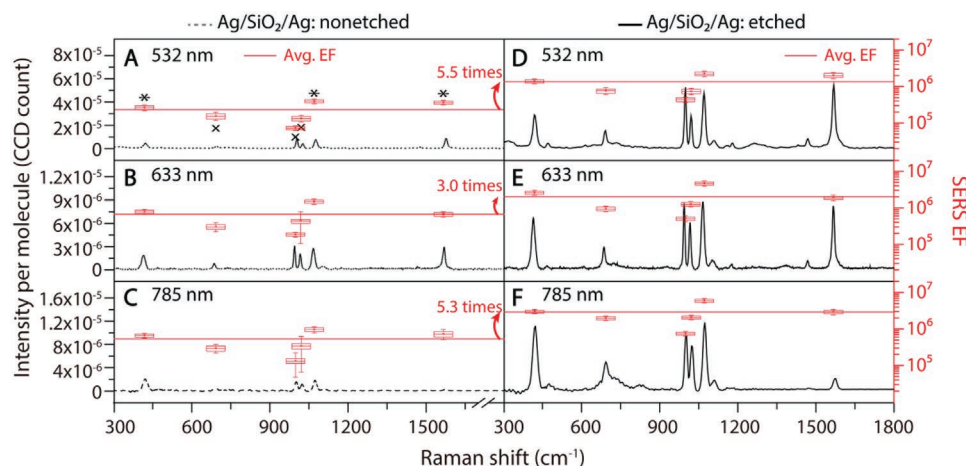


Figure 2. Multi-band SERS performance of Ag/SiO₂/Ag nanolaminate plasmonic nanocavities on vertical nanopillars. A–C) The average SERS spectra and corresponding SERS EFs of different BZT Raman peaks from the sample before BOE etching under 532 nm (A), 633 nm (B), and 785 nm (C) excitations. D–F) The average SERS spectra and corresponding SERS EFs of different BZT Raman peaks from the sample after 15 s BOE etching under 532 nm (D), 633 nm (E), and 785 nm (F) excitations. The error bars show one standard deviation from 1200 pixels over three 20 μm × 20 μm regions. The bars in boxes from top to bottom represent 75th quartile, median, and 25th quartile values from 1200 pixels. The square represents the mean value.

benzenethiol (BZT) monolayer, a nonresonant Raman probe molecule.^[20] Figure 2A–C shows the averaged BZT SERS spectra from 1200 pixels over three 20 μm × 20 μm regions on the nonetched Ag/SiO₂/Ag sample under 532, 633, and 785 nm excitations, respectively. We determined SERS EFs for BZT vibrational modes at 422, 700, 1001, 1026, 1077, and 1576 cm^{−1} by the formula: $\text{SERS EF} = (I_{\text{SERS}}/N_{\text{SERS}})/(I_{\text{Raman}}/N_{\text{Raman}})$, where I_{SERS} , I_{Raman} , N_{SERS} , and N_{Raman} are the BZT SERS intensity, neat BZT Raman intensity, and the number of BZT molecules contributing to BZT SERS and neat BZT Raman intensities, respectively. According to the electromagnetic enhancement mechanism, the SERS EF for a molecule inside a hotspot can be expressed as

$$\text{SERS EF}(\omega_0 - \Delta\omega_m) = g(\omega_0)^2 \times g(\omega_0 - \Delta\omega_m)^2 \times \eta_m \quad (1)$$

where ω_0 is excitation laser frequency, $\Delta\omega_m$ is Stokes-shifted frequency for a specific vibrational mode, g is the local electric field enhancement factor, and η_m is the coefficient related to the orientation of transition dipole moment for a specific vibrational mode regarding the direction of the local electric field. We can find several vital points from experimentally determined SERS EFs for different BZT Raman modes. First, the values of SERS EFs vary between different BZT Raman peaks under the same laser excitation wavelength. For example, under 532 nm laser excitation, SERS EFs for 422, 1077, and 1576 cm^{−1} (marked by an asterisk in Figure 2A) are higher than those for 700, 1001, and 1026 cm^{−1} (marked by a cross in Figure 2A). This observation reveals that different vibrational modes undergo different SERS EFs due to the difference in their orientation related coefficients η_m . Considering the immobilized orientation of densely packed BZT monolayer on Ag surface,^[21] not all vibrational modes can be equally enhanced, and the vibrational modes perpendicular to the Ag surface are more enhanced than the vibrational modes in parallel with the Ag surface. By averaging the SERS EFs among different peaks, we can reduce the molecular orientation effect to approximate the plasmonic

local field enhancement factor $g(\omega_0)^2 \times g(\omega_0 - \Delta\omega_m)^2$. Accordingly, we obtain an average SERS EFs of $(2.3 \pm 0.2) \times 10^5$, $(6.6 \pm 1.0) \times 10^5$, and $(5.3 \pm 0.9) \times 10^5$ under 532, 633, and 785 nm excitations, respectively. The uncertainties are one standard deviation obtained from 1200 individual pixels. Second, the SERS EFs are different for the same vibrational mode under different excitation laser wavelengths, revealing the spectrally dispersive nature of the local field enhancement factor $g(\omega_0)^2 \times g(\omega_0 - \Delta\omega_m)^2$ associated with the multiresonant properties of plasmonic nanostructures. Figure 2D–F shows the BZT SERS spectra and SERS EFs for different BZT Raman peaks from BOE etched Ag/SiO₂/Ag samples under different laser excitation wavelengths. The average SERS EFs of etched Ag/SiO₂/Ag samples are $(1.3 \pm 0.2) \times 10^6$, $(2.0 \pm 0.3) \times 10^6$, and $(2.8 \pm 0.3) \times 10^6$ under 532, 633, and 785 nm excitations, which are approximately 5.5 ± 1.1, 3.0 ± 0.6, and 5.3 ± 1.1 times as high as SERS EFs for nonetched samples under associated laser excitations, respectively. The uncertainties are one standard deviation based on the propagation of uncertainties from 1200 individual pixels. This observation reveals that more hotspots in the nanogaps become accessible to analytes contributing to an improved SERS EF. These newly exposed resonant nanogap SERS hotspots on vertical nanopillars can be engulfed by cell membrane to enable effective multi-band SERS molecular profiling of membrane protein biomarkers in biomedical applications.

To examine the spatial uniformity of multi-band SERS responses for the Ag/SiO₂/Ag nanolaminate sample, we conducted 2D confocal Raman mapping over the same sample area under excitations at 532, 633, and 785 nm (Figure 3). As shown in Figure 3A, we created an L-shape imaging marker by photothermal burning under a high-power focused laser beam to allow accurate position registration in 2D Raman maps (yellow dashed square, 35 μm × 35 μm) measured under the three excitation wavelengths. Figure 3B–D illustrates the 2D maps of measured SERS EFs for the 1077 cm^{−1} BZT peak from the same sample area under 532, 633, and 785 nm excitations,

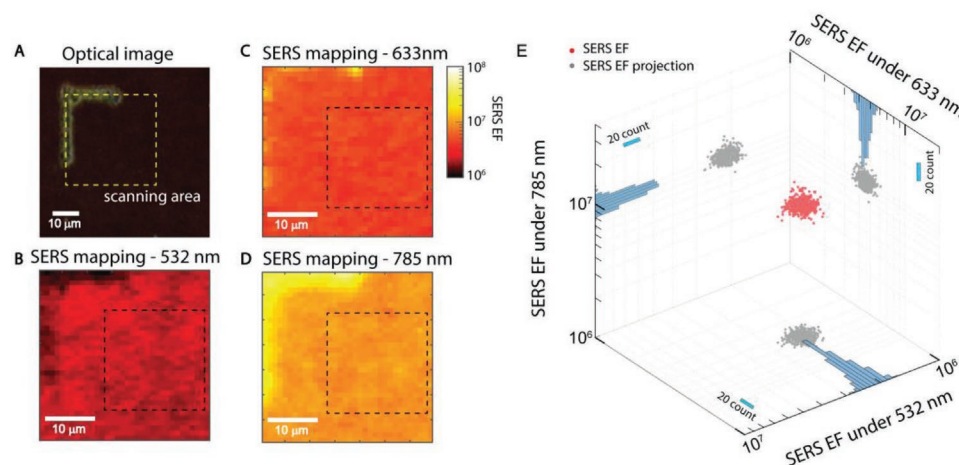


Figure 3. Uniform spatial distribution of multi-band SERS responses for Ag/SiO₂/Ag nanolaminate plasmonic nanocavities on vertical nanopillars. A) Bright-field optical image and B–D) scanning confocal SERS mapping images (at 1077 cm⁻¹) of the same region (marked as the yellow dashed square in (A)) from the sample after 15 s BOE etching under 532 nm (B), 633 nm (C) and 785 nm (D) excitations. E) The 3D scatter plot and histograms of SERS EFs for the BZT Raman peak at 1077 cm⁻¹ from individual laser beam locations within the black dashed region in (B–D) under 532, 633, and 785 nm excitations.

manifesting a uniform distribution for broadband high-performance SERS responses. Interestingly, the L-shaped marker region exhibits higher SERS EFs under 633 and 785 nm excitations and lower SERS EFs under 532 nm excitation than the rest because the geometric disruption from laser photothermal damage can change the multiresonant plasmonic properties. Figure 3E shows the SERS EF scatter plot and the histograms for the BZT 1077 cm⁻¹ Raman peak from 400 pixels within the same 20 μm × 20 μm area (black dashed square in Figure 3B–D) under 532, 633, and 785 nm excitations. The simultaneously high and uniform SERS EFs under three laser excitation wavelengths suggest that nanolaminate plasmonic nanostructures can support multiple resonant modes with spatial overlap within the optical diffraction limit (≈655 nm) in measurements.

To further investigate the multi-band SERS response within individual MIM nanogap, we created Ag/SiO₂/MgF₂/Ag nanolaminate plasmonic nanostructures consisting of MgF₂ and SiO₂ as two different insulator materials in MIM nanocavities (Figure 4A). Specifically, the bottom two insulator layers of MgF₂ are non-etchable by HF during the BOE wet etching process. Also, MgF₂ has a refractive index ranging from 1.37 to 1.39 in the vis–NIR range, slightly smaller than the refractive index of SiO₂ (1.45 to 1.48), and thus the optical properties of the nanolaminate plasmonic systems do not change a lot. As confirmed in the SEM images (Figure 4B), a 15 s BOE etching process can partially expose the nanogap embedded hotspots associated with the top SiO₂ layer but not those associated with the middle and bottom MgF₂ layers. To evaluate the optical near field enhancement associated with hotspots in the top SiO₂ nanogap, we measured SERS signals from BZT self-assembled Ag/SiO₂/MgF₂/Ag samples under the same experimental conditions as in Figure 2 for Ag/SiO₂/Ag samples. Before BOE etching, as shown in Figure 4C, BZT SERS signals from the Ag/SiO₂/Ag and Ag/SiO₂/MgF₂/Ag samples have similar intensities under 532, 633, and 785 nm excitations. According to Equation (1), Ag/SiO₂/Ag and Ag/SiO₂/MgF₂/Ag samples before BOE etching share the same molecule orientation coefficient

η_m , and their SERS EFs primarily depend on the optical near-field enhancement term of $g(\omega_0)^2 \times g(\omega_0 - \Delta\omega)^2$. Therefore, for Ag/SiO₂/Ag and Ag/SiO₂/MgF₂/Ag samples before BOE etching, their similar SERS intensities under different excitation wavelengths reveal their similar multiresonant plasmonic near-field enhancement responses in $g(\omega_0)^2 \times g(\omega_0 - \Delta\omega)^2$ before geometric changes by etching SiO₂ layers in nanogap. As shown in Figure 4D–F, after a 15 s BOE etching, the averaged SERS EFs of Ag/SiO₂/MgF₂/Ag samples increased to approximately 3.3 ± 0.5 , 2.6 ± 0.4 , and 3.5 ± 0.5 times compared to the nonetched sample under 532, 633, and 785 nm excitations, respectively. The uncertainties are one standard deviation based on the propagation of uncertainties from 1200 individual pixels. The partial exposure of the top nanogap embedded hotspots causes such multi-band SERS EF improvement under different excitation wavelengths over the vis–NIR spectral range.

While the SERS EF increment originates from the top nanogap hotspots for the Ag/SiO₂/MgF₂/Ag samples, the SERS EF increment comes from hotspots in all three nanogaps for the Ag/SiO₂/Ag samples. As shown in Figure 4G, the SERS EF increment of the Ag/SiO₂/Ag samples (outlined by the black rectangle) can be decomposed into the contributions from the top nanogap hotspots (orange box) and the rest of the middle and the bottom nanogap hotspots (light orange box). Suppose we approximate the SERS EF increment associated with the exposed top nanogap hotspots (orange box) in the Ag/SiO₂/Ag samples with the SERS EF increment contributed by top SiO₂ nanogap hotspots in the Ag/SiO₂/MgF₂/Ag samples, we can retrieve the relative ratio of SERS EF contributions among different nanogaps in the Ag/SiO₂/Ag samples. As shown in Figure 4G, under 532 and 785 nm excitations, the SERS EF contributions from the top nanogap hotspots are similar to the combination of middle and bottom nanogap hotspots. Nevertheless, under 633 nm excitation, the SERS EF contributions are dominantly from the top nanogap hotspots, indicating the significant dependence of the spatial mode distribution among the three MIM nanogaps on excitation laser wavelength.

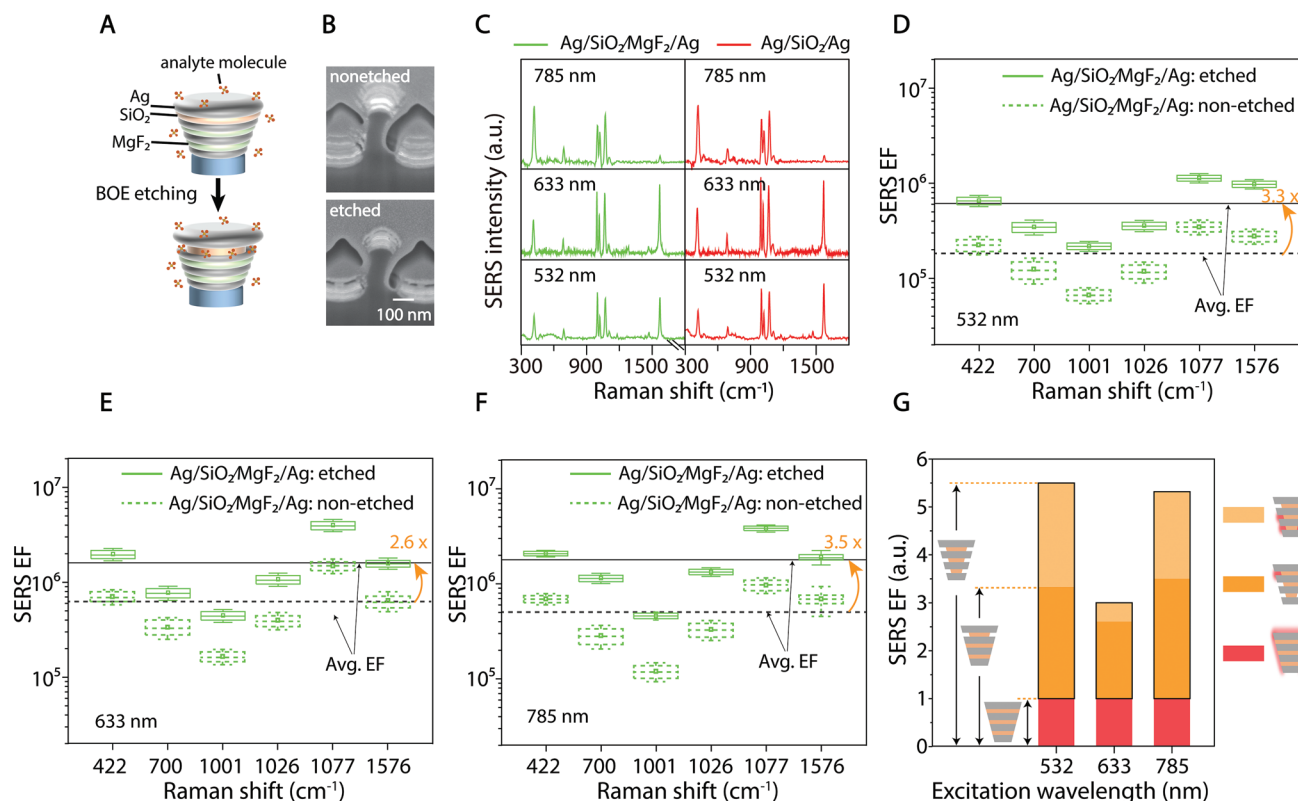


Figure 4. Multi-band SERS responses at a single MIM nanocavity level. A) Schematic illustration of BOE etching of SiO₂ layer in Ag/SiO₂/MgF₂/Ag nanolaminate plasmonic nanocavities on vertical nanopillars. B) The cross-sectional view SEM images of Ag/SiO₂/MgF₂/Ag sample before (nonetched) and after 15 s BOE etching of the SiO₂ layer. C) The measured SERS spectra of BZT molecules from Ag/SiO₂/MgF₂/Ag and Ag/SiO₂/Ag samples under 532, 633, and 785 nm excitations with an etching time of 0 s. D–F) The SERS EFs in box plots of different BZT Raman peaks from the Ag/SiO₂/MgF₂/Ag sample before (nonetched) and after 15 s BOE etching of the SiO₂ layer under 532 nm (D), 633 nm (E), and 785 nm (F) excitations. The error bars show one standard deviation from 1200 pixels over three 20 μ m \times 20 μ m regions. The bars in boxes from top to bottom represent 75th quartile, median, and 25th quartile values from 1200 pixels. The square represents the mean value. G) Normalized SERS EF increments after BOE etching of Ag/SiO₂/Ag (outlined by the black rectangle) and Ag/SiO₂/MgF₂/Ag (highlighted as orange) samples compared to nonetched samples (highlighted as red).

To investigate the multiresonant properties of nanolaminate plasmonic nanocavities on vertical nanopillars, we have measured far-field reflectance and transmittance spectra of Ag/SiO₂/Ag (Figure 5A and Figure S3A, Supporting Information) and Ag/SiO₂/MgF₂/Ag (Figure 5B and Figure S3B, Supporting Information) samples. The reflectance spectra (Figure 5A) of the Ag/SiO₂/Ag sample exhibit multiple dips at 435, 534, 623, 685, 706, and 919 nm. The Ag/SiO₂/MgF₂/Ag sample (Figure 5B) shows a similar reflectance spectrum with multiple dips at 435, 565, 662, 710, and 811 nm. This observation reveals that the minor refractive index change from SiO₂ (1.45 to 1.48) to MgF₂ (1.37 to 1.39) in nanogap layers has a limited effect on the multiresonant optical properties of nanolaminate plasmonic nanocavities on vertical nanopillars. Moreover, we have calculated the far-field and near-field optical properties using the finite-difference time-domain (FDTD) method. Our calculations illustrate that Ag/SiO₂/Ag and Ag/SiO₂/MgF₂/Ag samples exhibit similar reflectance spectra (red lines in Figure 5A,B) with multiple resonant dips, agreeing with the measurements. The measurements show resonant features with broader linewidths than the calculations. It should be noted that the reflectance spectra are measured over a spot size of 12.50 mm \times 7.11 mm containing 5.55×10^8 plasmonic nanopillar units. As seen in the SEM images (Figure 1 and Figure S1,

Supporting Information), the geometric variations between individual nanopillars and plasmonic nanocavities can cause the inhomogeneous broadening effect, leading to broader resonant linewidths in the measurements than FDTD simulations (Figure S4, Supporting Information). Moreover, the increased metal losses associated with the surface roughness can also cause the homogeneous broadening effect.

To understand the microscopic resonant behaviors, we calculated the optical response of the two subsystems, nanolaminate nanoparticle arrays (Figure 5C) and nanolaminate nanohole arrays (Figure 5D), in comparison with the coupled system (Figure 5E). Figure 5C shows that nanolaminate nanoparticle arrays support three dominant absorption peaks attributed to diffraction lattice mode at $\lambda_{\text{NPA}-1} \approx 447$ nm, the electric dipole (ED) mode at $\lambda_{\text{NPA}-2} \approx 543$ nm, and the magnetic dipole (MD) mode at $\lambda_{\text{NPA}-3} \approx 1047$ nm (Figure S5, Supporting Information). On the other hand, as shown in Figure 5D, nanolaminate nanohole arrays exhibit four absorption peaks associated with three bottom metal-polymer interface Bloch surface plasmon polariton (SPP) modes: $(\pm 2, \pm 2)$ at $\lambda_{\text{NHA}-1} \approx 425$ nm, $(\pm 1, \pm 1)$ at $\lambda_{\text{NHA}-2} \approx 515$ nm, and $(\pm 1, 0)$ at $\lambda_{\text{NHA}-3} \approx 704$ nm as well as one hybridized nanogap Bloch SPP mode $(\pm 1, \pm 1)$ at $\lambda_{\text{NHA}-4} \approx 971$ nm (Figure S6, Supporting

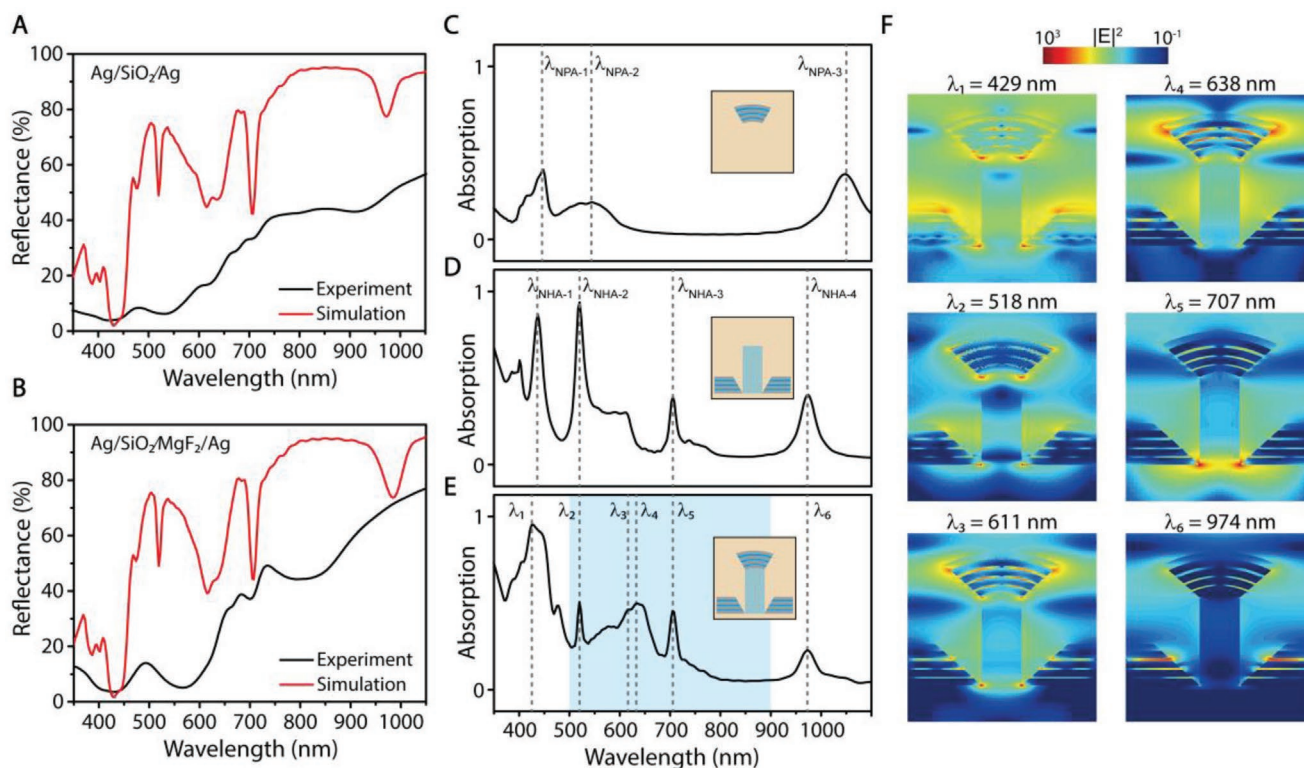


Figure 5. Far-field and near-field optical properties of the nanolaminate plasmonic nanocavities on vertical nanopillars. (A–B) Measured and FDTD-calculated reflectance spectra of (A) Ag/SiO₂/Ag and (B) Ag/SiO₂/MgF₂/Ag samples. (C–E) The FDTD-calculated absorption spectra for the two subsystems of (C) Ag/SiO₂/Ag nanolaminate nanoparticle array and (D) Ag/SiO₂/Ag nanolaminate nanohole array in comparison with (E) the coupled system of the Ag/SiO₂/Ag sample. (F) FDTD-calculated x-z distribution maps of $|E|^2$ for plasmonic modes λ_1 – λ_6 marked in (E).

Information). For the coupled system of nanolaminate nanocavities on nanopillar arrays, as shown in Figure 5E, we can observe six absorption peaks at resonant wavelengths correlated with the modes in their subsystems of nanolaminate nanoparticle arrays and nanolaminate nanohole arrays, manifesting that their multiresonant responses originate from the plasmonic hybridization between elementary modes in the two subsystems in far-field coupling regime.^[22] FDTD-calculated near-field mode profiles in Figure 5F confirm that the modes in nanolaminate nanocavities on nanopillar arrays show mode distribution profiles with spatial correlation with elementary modes in their two uncoupled subsystems (Figure S7, Supporting Information). Specifically, the hybrid mode at λ_1 exhibits a relatively weak field enhancement due to the weak local field confinement of the lattice plasmon mode ($\lambda_{\text{NPA}-1}$) and weak coupling efficiency with free-space light of the high order Bloch SPP mode ($\lambda_{\text{NHA}-1}$). The hybrid modes at λ_2 , λ_3 , and λ_4 show concentrated electric field inside the insulator layers of the nanolaminate nanoparticles since the ED localized surface plasmon (LSP) mode ($\lambda_{\text{NPA}-2}$) is strongly excited by the spectrally well-aligned Bloch SPP mode ($\lambda_{\text{NHA}-2}$) through the far-field coupling. In contrast, the hybrid mode at λ_5 is weakly excited at the nanolaminate nanoparticle part but concentrated at the bottom of the nanolaminate nanohole arrays because the off-resonant ED LSP mode ($\lambda_{\text{NPA}-2}$) only weakly couples with the on-resonant Bloch SPP mode ($\lambda_{\text{NHA}-3}$). The hybrid mode at λ_6 is mainly located in the insulator layers in nanolaminate nanohole arrays since the MD LSP mode ($\lambda_{\text{NPA}-3}$) is weakly excited

through far-field coupling due to its low quantum yield compared to the hybridized Bloch SPP mode ($\lambda_{\text{NHA}-4}$). Across the spectral range in multi-band SERS measurements between 500 and 900 nm (shaded with blue in Figure 5E), the multiresonant features are primarily associated with the hybrid modes λ_2 to λ_5 , where the molecule-accessible nanogap hotspots are primarily in nanolaminate nanocavities on vertical nanopillars. Notably, the nanolaminate plasmonic nanoparticle array with increased pitch sizes can still have the multiresonant responses with substantial local field enhancement due to the hybridization between localized plasmonic modes in the stacked MIM building blocks with different insulator thicknesses.^[23] This feature also benefits SERS analysis of living cells because a low lattice density of the vertical nanopillar arrays will promote stable cell adhesion and trigger cells into a less motile state,^[24] facilitating direct SERS molecular profiling of membrane protein biomarkers.

To understand the difference of spatial mode distribution between three insulator nanogaps in nanolaminate nanocavities on vertical nanopillars, we conducted FDTD simulations with three center-to-edge line monitors placed within three individual nanogaps (Figure 6A). As depicted in Figure 6B–D, the mode profiles ($|E|^2$) show a spectral dispersion in each nanogap. Interestingly, the spectral dispersion behaves differently in each nanogap. Specifically, from 600 to 700 nm the $|E|^2$ distributes unimodally in the top nanogap but bimodally in the middle and bottom nanogaps, as the dashed lines noted, revealing different mode natures in these three nanocavities. In the bottom

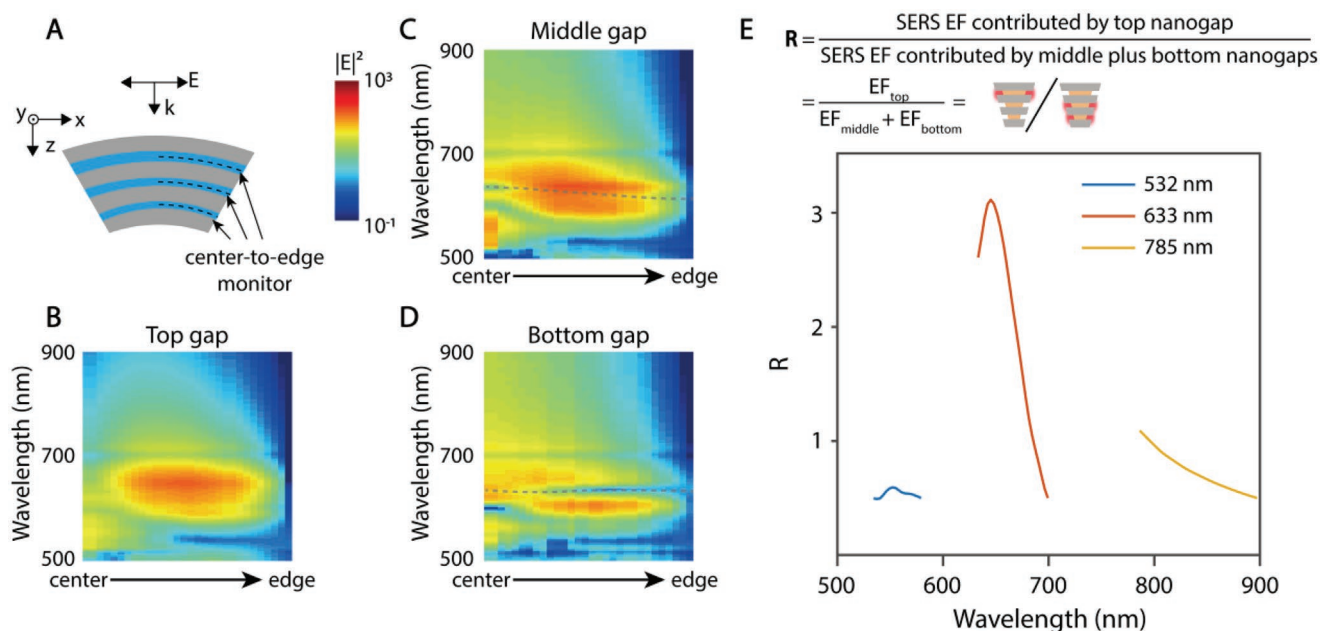


Figure 6. Near-field optical field enhancement inside MIM nanogaps. (A) Schematic of Ag/SiO₂/Ag nanolaminate plasmonic nanocavities on vertical nanopillars with curved center-to-edge monitors under the polarized light illumination. (B–D) The FDTD-calculated spectral maps of near-field $|E|^2$ enhancement factor as a function of radial position from the center to the edge on the curved line monitor within (B) top, (C) middle, and (D) bottom nanogaps in the Ag/SiO₂/Ag sample. (E) The ratio of calculated SERS enhancement factors between the top nanogap and the combination of middle and bottom nanogaps in the Ag/SiO₂/Ag sample.

nanogap, there is a phase flip of the electric field across 600 to 700 nm (Figure S8, Supporting Information), resulting in a transition from a magnetic quadrupole (MQ) LSP mode to MD LSP mode and consequently the bimodal characteristics of the $|E|^2$ profile in the middle and bottom nanogaps. In contrast, the fields inside the top nanogap maintain the MD mode nature with a unimodal $|E|^2$ distribution across 600 to 700 nm. We further quantified the SERS EF contributed by each nanogap as

$$EF_i(\lambda_0, \lambda) = \sum_j |r_j| \left| \frac{E(\mathbf{r}_j, \lambda_0)}{E_0(\mathbf{r}_j, \lambda_0)} \right|^2 \left| \frac{E(\mathbf{r}_j, \lambda)}{E_0(\mathbf{r}_j, \lambda)} \right|^2 \quad (2)$$

where i is the notation of the gap, λ_0 is the excitation wavelength, λ is the emission wavelength, \mathbf{r}_j is the position vector in the specific insulator gap with an estimated etching depth (10 nm) from the gap edge, and the $|r_j|$ is the weight related to the molecule adsorption surface area. The enhancement factor ratio between the top nanogap and combination of the middle and bottom nanogaps can be approximated as $R = EF_{\text{top}}(\lambda_0, \lambda) / [EF_{\text{middle}}(\lambda_0, \lambda) + EF_{\text{bottom}}(\lambda_0, \lambda)]$ as plotted in Figure 6E. The ratio, R , is spectrally dispersive and higher at 633 nm than at 532 and 785 nm, agreeing with our experimental observations (Figure 4G).

3. Conclusion

In summary, we demonstrate that MIM nanolaminate plasmonic nanocavities on high-aspect-ratio nanopillar arrays can achieve high SERS EFs ($>10^6$) over a broad spectral range (500 to 900 nm) with multiresonant optical concentration at the single nanocavity

level. Such nanolaminate plasmonic nanostructures can provide a multi-band uniform and reproducible SERS signal with a small footprint by accurate nanoscale control of vertically oriented plasmonic nanogap geometries, desirable for multi-band SERS applications. Our measurements and calculations reveal that the individual nanolaminate nanocavities can support multiple resonance modes over a broad wavelength range with substantial near-field enhancement. The multiresonant nanolaminate plasmonic nanostructures can allow multi-band SERS/SERS operation under different laser excitations from 500 to 900 nm, potentially enabling high-dimensional biochemical analyses by providing combined electronic and vibrational molecular information. Furthermore, nanolaminate plasmonic nanocavities can easily integrate with vertical nanopillar electrode arrays for combined electrical recording and SERS monitoring of living cells. Beyond multi-band SERS applications, multiresonant nanolaminate substrates can serve as wavelength-multiplexed multifunctional plasmonic nanotransducers at the subcellular level with different optical modalities. Our studies suggest that nanolaminate plasmonic nanostructures on high-aspect-ratio nanopillar arrays can allow the simultaneous nanolocalized enhancement of both excitation and emission transitions in multiphoton nonlinear processes across a broad wavelength range, opening exciting avenues toward cell-interfaced nonlinear nano-optics sensing/spectroscopy/imaging applications.

4. Experimental Section

Sample Fabrication: A composite PDMS stamp was replicated from a Si master with vertical nanopillar arrays (100 nm in diameter, 400 nm in

height, and 400 nm in period) by soft lithography.^[25] Then, a UV-curable polyurethane (PU) nanopillar array was replicated on a polyester film from the PDMS stamp by UV curing for 5 min, followed by heat-curing at 80 °C overnight. Next, alternative Ag and SiO₂ (or MgF₂) thin films were deposited on the PU nanopillar arrays by physical vapor evaporation with designed thickness. Also, 1 nm thick Cr between polymer nanopillar array and the first Ag layer, and 0.7 nm thick Ti between metal and insulator layers were deposited to improve the adhesion.

SERS Characterization: A confocal Raman microscope equipped with 532, 633, and 785 nm lasers was used for multi-band SERS measurement. To form a BZT monolayer, the SERS substrates were incubated in 1 mol m⁻³ BZT ethanolic solution for 24 h, followed by ethanol rinsing. Back-scattered Raman signals were collected via a 20× objective (NA = 0.4) with 0.1 s integration time. The laser power intensities were 0.1, 0.1, and 2 mW for 532, 633, and 785 nm measurements, respectively.

SERS EF Calculation: SERS EFs were calculated by $SERS\ EF = (I_{SERS}/N_{SERS})/(I_{Raman}/N_{Raman})$, where I_{SERS} , I_{Raman} , N_{SERS} , N_{Raman} are the BZT SERS intensity, neat BZT Raman intensity, and the number of BZT molecules contributing to BZT SERS and neat BZT Raman intensities, respectively.^[26] N_{SERS} was calculated by $N_{SERS} = SA \times \rho_{SERS}$, where SA is the metal surface area contributing to the SERS enhancement, and ρ_{SERS} is the molecule packing density of BZT monolayer on the Ag NP surface (3.3×10^{14} cm⁻²).^[27] N_{Raman} was calculated with $N_{Raman} = A \times d_{eff} \times \rho_{BZT}$, where A is the focused laser beam area, d_{eff} is the effective depth of the laser beam spot under 20× objective, and ρ_{BZT} is the neat BZT molecule density (5.9×10^{21} cm⁻³). For I_{SERS} and I_{Raman} , six major Raman peaks at 422, 700, 1001, 1026, 1077, and 1576 cm⁻¹ were selected to calculate the SERS EF, which corresponded to the carbon–sulfur (C–S) stretching and carbon–carbon–carbon (C–C–C) ring in-plane deformation vibration, C–C–C ring in-plane bending with C–S stretching mode, the C–C–C ring in-plane bending mode, the carbon–hydrogen (C–H) in-plane bending mode, the C–C–C ring in-plane breathing mode with C–S stretching mode, and the C–S stretching mode for BZT molecules.^[28]

Far-Field Reflectance and Transmittance Measurement: The reflectance and transmittance spectra of samples were measured by a UV–vis–near-infrared (NIR) spectrophotometer. In reflectance measurement, the specular and diffuse reflections were collected by an integrating sphere with an incidence angle of 3.33°.

Numerical Simulations: A cone-shape nanoparticle and a beveled nanohole were adopted to mimic the shadowing effect in the deposition. A uniform mesh size of 1 nm (in x, y, and z directions) was used. The Bloch boundary condition was used in x- and y-directions with a periodicity of 400 nm, and the perfectly matched layer boundary condition was used in the z-direction. A normal-incident plane wave source was used to mimic the incidence angle in far-field reflectance measurement. The dielectric function of silver was obtained from the Palik handbook of optical constants for solids.^[29]

Supporting Information

Supporting Information is available from the Wiley Online Library or from the author.

Acknowledgements

M.N. and Y.Z. contributed equally to this work. This work was partially supported by US AFOSR Young Investigator Award FA9550-18-1-0328, US NSF grant DMR2139317, US NIST grant 70NANB18H201, and US NIST grant 70NANB19H163.

Conflict of Interest

The authors declare no conflict of interest.

Data Availability Statement

The data that support the findings of this study are available from the corresponding author upon reasonable request.

Keywords

multi-band surface-enhanced Raman spectroscopy, multiresonant plasmonics, nanolaminate plasmonics, spatial mode overlap, surface-enhanced Raman spectroscopy

Received: February 24, 2022

Revised: May 7, 2022

Published online: May 18, 2022

- [1] a) J. Langer, D. J. de Aberasturi, J. Aizpurua, R. A. Alvarez-Puebla, B. Auguie, J. J. Baumberg, G. C. Bazan, S. E. Bell, A. Boisen, A. G. Brolo, J. Choo, D. Cialla-May, V. Deckert, L. Fabris, K. Faulds, F. J. Garcia de Abajo, R. Goodacre, D. Graham, A. J. Haes, Christy L. Haynes, C. Huck, T. Itoh, M. Käll, J. Kneipp, N. A. Kotov, H. Kuang, E. C. Le Ru, H. K. Lee, J.-F. Li, X. Y. Ling, et al., *ACS Nano* **2019**, *14*, 28; b) S. Schlucker, *Angew. Chem., Int. Ed.* **2014**, *53*, 4756; c) C. Zong, M. X. Xu, L. J. Xu, T. Wei, X. Ma, X. S. Zheng, R. Hu, B. Ren, *Chem. Rev.* **2018**, *118*, 4946.
- [2] a) J. F. Li, Y. F. Huang, Y. Ding, Z. L. Yang, S. B. Li, X. S. Zhou, F. R. Fan, W. Zhang, Z. Y. Zhou, D. Y. Wu, B. Ren, Z. L. Wang, Z. Q. Tian, *Nature* **2010**, *464*, 392; b) C. Matricardi, C. Hanske, J. L. Garcia-Pomar, J. Langer, A. Mihi, L. M. Liz-Marzán, *ACS Nano* **2018**, *12*, 8531; c) V. K. Rao, T. P. Radhakrishnan, *ACS Appl. Mater. Interfaces* **2015**, *7*, 12767.
- [3] a) B. R. Lutz, C. E. Dentinger, L. N. Nguyen, L. Sun, J. Zhang, A. N. Allen, S. Chan, B. S. Knudsen, *ACS Nano* **2008**, *2*, 2306; b) J. A. Dougan, K. Faulds, *Analyst* **2012**, *137*, 545; c) W. E. Smith, *Chem. Soc. Rev.* **2008**, *37*, 955.
- [4] a) G. McNay, D. Eustace, W. E. Smith, K. Faulds, D. Graham, *Appl. Spectrosc.* **2011**, *65*, 825; b) H. Cho, B. R. Baker, S. Wachsmann-Hogiu, C. V. Pagba, T. A. Laurence, S. M. Lane, L. P. Lee, J. B.-H. Tok, *Nano Lett.* **2008**, *8*, 4386.
- [5] A. F. McGuire, F. Santoro, B. Cui, *Annu. Rev. Anal. Chem.* **2018**, *11*, 101.
- [6] a) M. D. Hodges, J. G. Kelly, A. J. Bentley, S. Fogarty, I. I. Patel, F. L. Martin, N. J. Fullwood, *ACS Nano* **2011**, *5*, 9535; b) H. Dong, D. Yao, Q. Zhou, L. Zhang, Y. Tian, *Chem. Commun.* **2019**, *55*, 1730; c) L. Xiao, K. A. Bailey, H. Wang, Z. D. Schultz, *Anal. Chem.* **2017**, *89*, 9091.
- [7] a) E. A. Vitol, Z. Orynbayeva, M. J. Bouchard, J. Azizkhan-Clifford, G. Friedman, Y. Gogotsi, *ACS Nano* **2009**, *3*, 3529; b) J. J. Niu, M. G. Schrlau, G. Friedman, Y. Gogotsi, *Small* **2011**, *7*, 540; c) A. Huefner, W.-L. Kuan, R. A. Barker, S. Mahajan, *Nano Lett.* **2013**, *13*, 2463.
- [8] a) W. Zhao, L. Hanson, H.-Y. Lou, M. Akamatsu, P. D. Chowdary, F. Santoro, J. R. Marks, A. Grassart, D. G. Drubin, Y. Cui, B. Cui, *Nat. Nanotechnol.* **2017**, *12*, 750; b) M. Dipalo, A. F. McGuire, H.-Y. Lou, V. Caprettini, G. Melle, G. Bruno, C. Lubrano, L. Matino, X. Li, F. De Angelis, B. Cui, F. Santoro, *Nano Lett.* **2018**, *18*, 6100; c) A. Hai, D. Kamber, G. Malkinson, H. Erez, N. Mazurski, J. Shappir, M. E. Spira, *J. Neural Eng.* **2009**, *6*, 066009; d) F. Santoro, S. Dasgupta, J. Schnitker, T. Auth, E. Neumann, G. Panaitov, G. Gompper, A. Offenhäusser, *ACS Nano* **2014**, *8*, 6713.
- [9] a) M. Dipalo, H. Amin, L. Lovato, F. Moia, V. Caprettini, G. C. Messina, F. Tantussi, L. Berdondini, F. De Angelis, *Nano*

- Lett.* **2017**, *17*, 3932; b) A. Cerea, V. Caprettini, G. Bruno, L. Lovato, G. Melle, F. Tantussi, R. Capozza, F. Moia, M. Dipalo, F. De Angelis, *Lab Chip* **2018**, *18*, 3492.
- [10] a) G. C. Messina, M. Dipalo, R. La Rocca, P. Zilio, V. Caprettini, R. P. Zaccaria, A. Toma, F. Tantussi, L. Berdondini, F. De Angelis, *Adv. Mater.* **2015**, *27*, 7145; b) J. J. Vandersarl, A. M. Xu, N. A. Melosh, *Nano Lett.* **2012**, *12*, 3881.
- [11] H. C. Jeon, C.-J. Heo, S. Y. Lee, S.-M. Yang, *Adv. Funct. Mater.* **2012**, *22*, 4268.
- [12] R. Liu, R. Chen, A. T. Elthakeb, S. H. Lee, S. Hinckley, M. L. Khraiche, J. Scott, D. Pre, Y. Hwang, A. Tanaka, Y. G. Ro, A. K. Matsushita, X. Dai, C. Soci, S. Biesmans, A. James, J. Nogan, K. L. Jungjohann, D. V. Pete, D. B. Webb, Y. Zou, A. G. Bang, S. A. Dayeh, *Nano Lett.* **2017**, *17*, 2757.
- [13] a) N. Shmoel, N. Rabieh, S. M. Ojovan, H. Erez, E. Maydan, M. E. Spira, *Sci. Rep.* **2016**, *6*, 27110; b) S. M. Ojovan, N. Rabieh, N. Shmoel, H. Erez, E. Maydan, A. Cohen, M. E. Spira, *Sci. Rep.* **2015**, *5*, 14100.
- [14] N. Zhang, K. Liu, Z. J. Liu, H. M. Song, X. Zeng, D. X. Ji, A. Cheney, S. H. Jiang, Q. Q. Gan, *Adv. Mater. Interfaces* **2015**, *2*, 1500142.
- [15] Y. Kalachyova, D. Mares, V. Jerabek, K. Zaruba, P. Ulbrich, L. Lapcak, V. Svorcik, O. Lyutakov, *J. Phys. Chem. C* **2016**, *120*, 10569.
- [16] P. Mao, C. Liu, G. Favraud, Q. Chen, M. Han, A. Fratalocchi, S. J. N. c. Zhang, *Nat. Commun.* **2018**, *9*, 5428.
- [17] N. Kazemi-Zanjani, M. Shayegannia, R. Prinja, A. O. Montazeri, A. Mohammadzadeh, K. Dixon, S. Zhu, P. R. Selvaganapathy, A. Zavodni, N. Matsuura, N. P. Kherani, *Adv. Opt. Mater.* **2018**, *6*, 1701136.
- [18] J. Song, W. Nam, W. Zhou, *Adv. Mater. Technol.* **2019**, *4*, 1800689.
- [19] S. A. S. Tali, W. J. N. Zhou, *Nanophotonics* **2019**, *8*, 1199.
- [20] a) N. G. Greeneltch, M. G. Blaber, G. C. Schatz, R. P. Van Duyne, *J. Phys. Chem. C* **2013**, *117*, 2554; b) X. Zhang, Y. Zheng, X. Liu, W. Lu, J. Dai, D. Y. Lei, D. R. Macfarlane, *Adv. Mater.* **2015**, *27*, 1090.
- [21] a) J. Nara, S. I. Higai, Y. Morikawa, T. Ohno, *J. Chem. Phys.* **2004**, *120*, 6705; b) S. K. Saikin, R. Olivares-Amaya, D. Rappoport, M. Stopa, A. Aspuru-Guzik, *Phys. Chem. Chem. Phys.* **2009**, *11*, 9401.
- [22] S. A. S. Tali, J. Song, W. Nam, W. Zhou, *Adv. Opt. Mater.* **2021**, *9*, 2001908.
- [23] a) Y. Z. Qian, S. A. S. Tali, E. Mejia, W. Zhou, *Optik* **2021**, *230*, 166332; b) E. Mejia, Y. Qian, S. A. S. Tali, J. Song, W. Zhou, *Appl. Phys. Lett.* **2021**, *118*, 241108; c) J. Song, W. Zhou, *Nano Lett.* **2018**, *18*, 4409.
- [24] H. Persson, Z. Li, J. O. Tegenfeldt, S. Oredsson, C. N. Prinz, *Sci. Rep.* **2015**, *5*, 18535.
- [25] D. Qin, Y. N. Xia, G. M. Whitesides, *Nat. Protoc.* **2010**, *5*, 491.
- [26] E. C. Le Ru, E. Blackie, M. Meyer, P. G. Etchegoin, *J. Phys. Chem. C* **2007**, *111*, 13794.
- [27] J. Y. Gui, D. A. Stern, D. G. Frank, F. Lu, D. C. Zapien, A. T. Hubbard, *Langmuir* **1991**, *7*, 955.
- [28] T. H. Joo, M. S. Kim, K. Kim, *J. Raman Spectrosc.* **1987**, *18*, 57.
- [29] E. D. Palik, *Handbook of Optical Constants of Solids*, Academic Press, Cambridge, MA **1998**.